



A dual full-bridge series-series resonant IPT system for ultra-wide-range electric vehicle battery applications

Marupuru Vinod¹ · Dharavath Kishan¹

Received: 2 January 2024 / Accepted: 10 June 2024

© The Author(s), under exclusive licence to Springer-Verlag GmbH Germany, part of Springer Nature 2024

Abstract

The design of inductive charging systems presents a significant challenge for various electric vehicle models, each equipped with diverse battery packs ranging from 200 to 800 V. Typically, DC–DC converters, along with diode bridge rectifiers or controlled rectifiers, are employed to accommodate this wide battery voltage range. However, this conventional approach increases vehicle weight and introduces greater control intricacies. In response, this article proposes a wide-gain converter with two sets of coupled coils to charge batteries of different voltage ranges without compromising system efficiency. The proposed system operates in four modes: voltage doubler mode, current doubler mode, full-bridge mode, and half-bridge mode, which has high voltage gain, high current gain, medium voltage gain, and low voltage gain operations. The simulations have been performed using MATLAB-Simulink software to validate the efficacy of the dual full-bridge converter across various battery voltages (800 V, 400 V, and 200 V) and power levels. Furthermore, a laboratory prototype has been built with SiC devices to further validate the proposed converter.

Keywords Battery pack voltage · Electric vehicle · Inductive charging system · DC–DC converter

1 Introduction

Inductive Power Transfer (IPT) stands as a transformative technology with wide-ranging applications spanning portable electronics, telecommunications, healthcare, and electric vehicle (EV) charging [1–3]. Particularly within the realm of EV charging, IPT emerges as a solution to prevalent issues such as driver inconvenience and safety concerns [4, 5]. The EV market boasts a diverse array of models, each featuring varying battery nominal voltages, typically falling within the range of 200 V to 800 V [6]. Presently, the majority of EVs are outfitted with batteries ranging from 300 to 400 V, largely due to the accessibility of precise auto-qualified components tailored for this voltage range. However, a notable shift is underway toward the adoption of 800V batteries [7], driven by significant benefits such as reduced wire gauge, minimized thermal losses, and faster charging times.

In the context of public charging infrastructure, encompassing locations like parking facilities, shopping malls,

highway rest areas, and shared charging stations, the efficient charging of EVs featuring different voltage-range batteries becomes imperative. Notably, leading automotive manufacturers such as Mercedes, Kia, Tesla's Model S, and Polestar primarily employ the 400V battery architecture, while counterparts like Hyundai IONIQ 5, Porsche Macan 4, and Xiaomi SU7 opt for the 800V battery architecture. This landscape underscores the necessity for charging solutions capable of accommodating varying voltage requirements across the EV spectrum.

In general, the straightforward approach involves designing various IPT systems tailored to different voltage-rated batteries. The reconfiguration of compensation circuits, transmitter, and receiver coils [8, 9] aims to accommodate varying battery pack voltages. However, it is important to note that this method contradicts the generalized design principles of any system. An alternative involves employing additional DC–DC converters in conjunction with the diode bridge rectifier to achieve a broad voltage range while maintaining the same power level. Despite yielding wide output voltages, this method compromises the overall system efficiency due to the introduction of extra DC–DC converters. Moreover, it escalates both the cost and complexity of the onboard charger, rendering it an unfeasible option.

✉ Dharavath Kishan
kishand@nitk.edu.in

¹ Department of Electrical and Electronics Engineering,
National Institute of Technology Karnataka, Surathkal, India

The other feasible option is to get a wide voltage range by applying variable and fixed frequency control techniques to the converters like LCC and CLLC. The variable frequency control [10–12] offers the advantage of achieving a broad spectrum of output voltages. Nevertheless, employing this control technique can introduce complexities when designing a suitable filter to accommodate such a wide range. Challenges like managing electromagnetic interference (EMI) and ensuring stability may also come to the forefront. The fixed frequency control [13–19], such as phase shift, asymmetrical duty cycle control, and asymmetrical clamped mode control techniques, can achieve a wide range in output voltage. However, in this method, the converter loses the soft switching, which impacts the system's overall efficiency.

The authors propose a resonant inductor-integrated transformer method [15] as a solution for charging batteries with different voltage requirements. However, this approach necessitates additional high-frequency transformers and increases the number of diodes and passive components on the secondary side, consequently adding to the onboard weight of the vehicle. In [20], another innovative approach is introduced by the author—the V-D/I-D converter, specifically designed for charging batteries rated at 400 V and 800 V. Nonetheless, this converter requires an augmented number of switches on the primary side. Despite these efforts, as outlined in [14, 20], scant research exists in the current literature on EV wireless charging systems capable of efficiently catering to both 400V and 800V batteries with equal power provisioning. This gap underscores the need for further exploration and innovation in the field to address the evolving demands of electric vehicle technology.

To address the aforementioned issues, this article proposes dual-coupled coils series-series resonant converter to get wide voltage and current gain with reduced switch count. Moreover, the proposed converter is free from secondary side control. The operating modes and mathematical modes of the proposed dual-coupled coil series-series resonant converter are described in Section II. MATLAB-Simulation results are provided in Section III, and hardware outcomes are elaborated in Section IV; finally, the conclusions are provided in Section V.

2 Proposed dual full-bridge series-series resonant converter

Figure 1 illustrates the configuration of the proposed converter. The primary side of the circuit comprises a high-frequency inverter (S_1 – S_6), a single-pole double-throw switch (SPDT), two primary side coils (L_1 and L_2) with associated equivalent series resistances (R_1 and R_2), and primary side resonant capacitors (C_1 and C_2). The secondary side comprises of two secondary coils (L_3 and L_4) with equivalent series resistances (R_3 and R_4), a bridge rectifier (D_1 – D_6), and secondary side resonant capacitors (C_3 and C_4). Additionally, filter capacitor (C_0) is incorporated. The detailed design calculations of coils and tuning parameters are given in [21]. Based on gating signals applied to the high-frequency inverter and SPDT switch position, the proposed dual-coil series-series resonant converter operates in four modes: (i) Voltage doubler mode (V-D), (ii) Current doubler mode (I-D), (iii) Full-bridge mode (F-B), and (iv) Half-bridge mode (H-B).

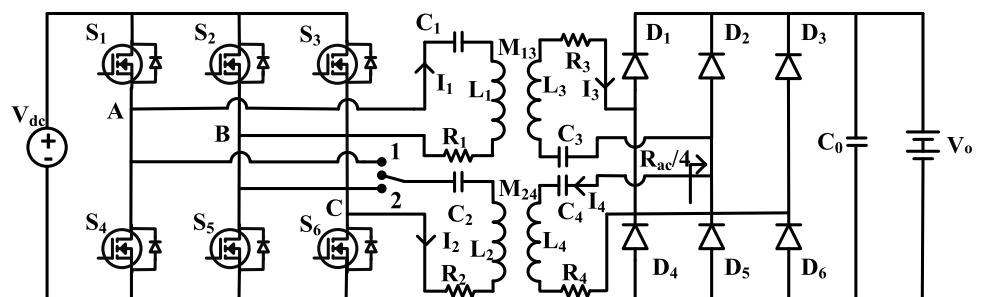
2.1 Voltage doubler mode

In V-D mode, the position of the SPDT switch is connected to position 1. Figure 2a illustrates the synchronization of gating pulses for switches S_5 and S_6 with S_1 and complimentary to the other switches with a 0.5-duty ratio, forming two separate full bridges. The equivalent circuit for V-D mode is presented in Fig. 3a. On the secondary side, diodes D_2 and D_5 remain in a permanently inactive state during this mode. This setup effectively establishes a series connection among the two coils and the load. Consequently, the voltage across the load equals the cumulative sum of the voltages across the secondary coils.

2.2 Current doubler mode

In I-D mode, the position of the SPDT switch is connected to position 2. Figure 2b illustrates the synchronization of gating pulses for switches S_3 and S_5 with S_1 and complimentary to the other switches with a 0.5-duty ratio, forming two separate full bridges. The equivalent circuit for I-D mode is presented

Fig. 1 Proposed dual full-bridge S–S resonant converter



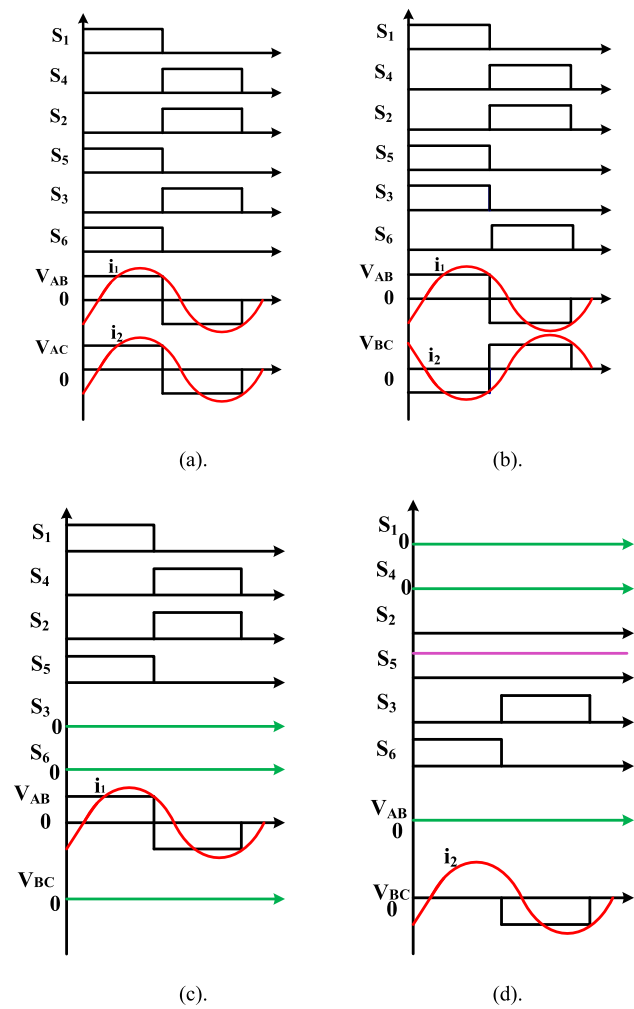


Fig. 2 Gating schemes of the proposed converter under different modes: **a** V-D mode, **b** I-D mode, **c** F-B mode, and **d** H-B mode

in Fig. 3b. On the secondary side, the diodes D_1 , D_3 , and D_5 are turned on in a positive cycle, and D_4 , D_2 , and D_6 are turned on in a negative half cycle, effectively establishing a parallel connection between the two coils and the load. As a consequence, the current across the load is the cumulative sum of the current passing through the secondary coils.

2.3 Full-bridge mode

The F-B mode can be implemented in two different configurations. Figure 2c presents the respective gating pulses for this mode. In the top coil utilization, switches S_3 and S_6 remain permanently turned off, while on the secondary side, diodes D_3 and D_6 are disabled. The equivalent circuit for this configuration is depicted in Fig. 4a. On the other hand, in the bottom coil utilization, switches S_1 and S_4 are permanently turned off, and diodes D_1 and D_4 on the secondary side are deactivated.

2.4 Half-bridge mode

The H-B mode can be implemented in two different configurations. Figure 2d presents the respective gating pulses for this mode. In the top coil utilization, switches S_1 , S_3 , and S_6 remain permanently turned off, and S_4 is permanently turned on, while on the secondary side, diodes D_3 and D_6 are disabled. The equivalent circuit for this configuration is depicted in Fig. 4b. On the other hand, in the bottom coil utilization, switches S_1 , S_4 , and S_2 are permanently turned off, and S_5 is permanently turned on, while diodes D_1 and D_4 on the secondary side are deactivated.

2.5 System Model

For simplification of analysis, the battery, filter capacitor, and diode bridge rectifier were replaced with the equivalent resistance (R_{ac}) given in (1).

$$R_{ac} = \frac{8}{\pi^2} \frac{V_{bat}^2}{P_{out}} \quad (1)$$

The diagonal distance between the coils is larger than the diameter of the coil, so the cross-coupling among the coils is almost negligible. In the case of V-D mode, by applying the Kirchhoff voltage law (KVL) to Fig. 2, one can obtain (2), (3), and (4).

$$V_{AB} - I_1 Z_1 - j I_3 \omega M_{13} = 0 \quad (2)$$

$$V_{AC} - I_2 Z_2 - j I_4 \omega M_{24} = 0 \quad (3)$$

$$j \omega M_{13} I_1 + j \omega M_{24} I_2 + (Z_4 + Z_3 + R_{ac}) I_3 = 0 \quad (4)$$

For easy analysis, the impedance of the resonant circuit is labeled as Z_1 , Z_2 , Z_3 , and Z_4 . After simplification, I_1 and I_2 have been derived in terms of system parameters given in (5) and (6) for voltage doubler mode.

$$I_1 = \frac{V_{AB}}{Z_1 + \left(\frac{\omega^2}{Z_4 + Z_3 + R_{ac}} \left(M_{13}^2 + \frac{Z_1}{Z_3} M_{13} M_{24} \right) \right)} \quad (5)$$

$$I_2 = \frac{V_{AC}}{Z_2 + \left(\frac{\omega^2}{Z_4 + Z_2 + R_{ac}} \left(M_{24}^2 + \frac{Z_2}{Z_1} M_{13} M_{24} \right) \right)} \quad (6)$$

For the case I-D mode, by applying KVL to Fig. 1, one can obtain the (7), (8), (9), and (10).

$$V_{AB} - I_1 Z_1 - j I_3 \omega M_{13} = 0 \quad (7)$$

$$V_{BC} - I_2 Z_2 - j I_4 \omega M_{34} = 0 \quad (8)$$

Fig. 3 Proposed converter operation: **a** voltage doubler and **b** current doubler mode

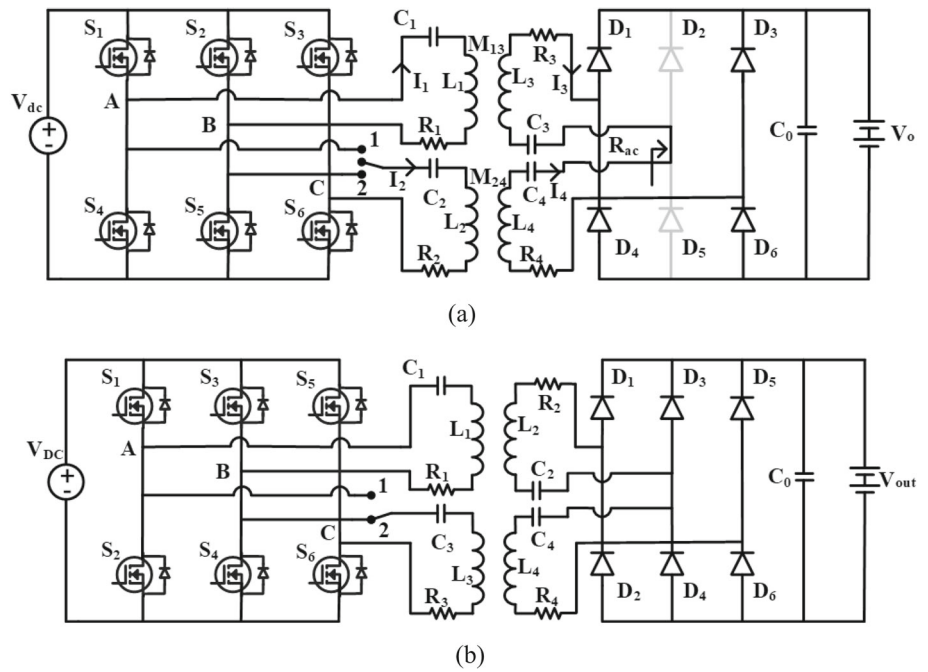
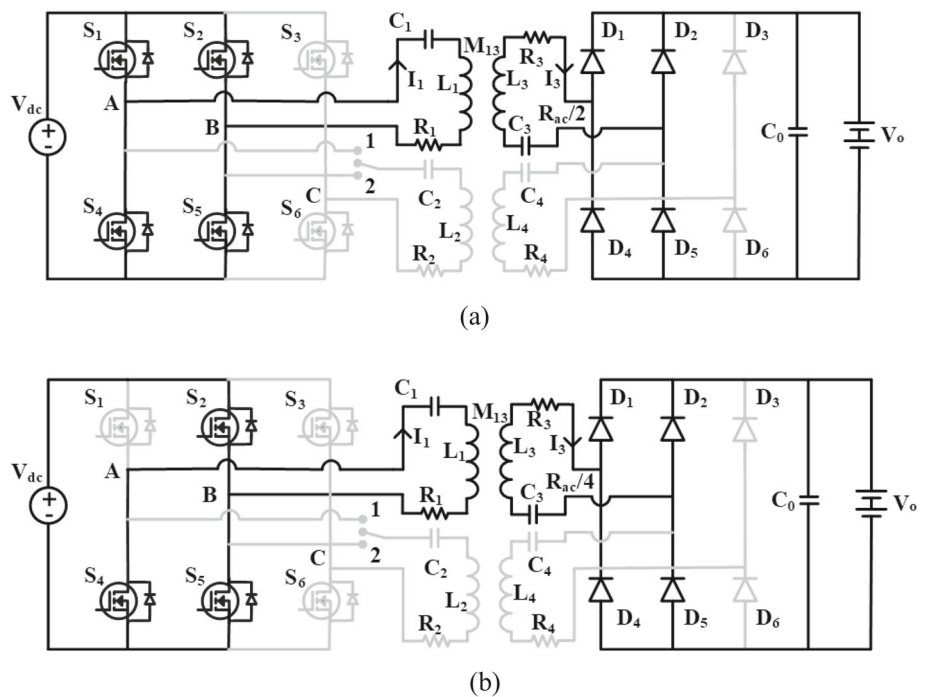


Fig. 4 Proposed converter operation: **a** full-bridge and **b** half-bridge mode



$$j\omega M_{13}I_1 + \left(Z_3 + \frac{R_{ac}}{4} \right) I_3 + \frac{R_{ac}}{4} I_4 = 0 \tag{9}$$

$$I_1 = \frac{V_{AB}}{Z_1 + \frac{M_{13}^2 \omega^2}{Z_3 + \frac{R_{ac}}{4} + \frac{Z_4 R_{ac}}{Z_3}}} \tag{11}$$

$$j\omega M_{24}I_2 + \left(Z_4 + \frac{R_{ac}}{4} \right) I_4 + \frac{R_{ac}}{4} I_3 = 0 \tag{10}$$

$$I_2 = - \frac{V_{BC}}{Z_2 + \frac{M_{24}^2 \omega^2}{Z_4 + \frac{R_{ac}}{4} + \frac{Z_3 R_{ac}}{Z_4}}} \tag{12}$$

The primary currents I_1 and I_3 for I-D mode are given in (11) and (12).

In the case of full-bridge mode, by applying KVL to Fig. 4, one can obtain (13) and (14).

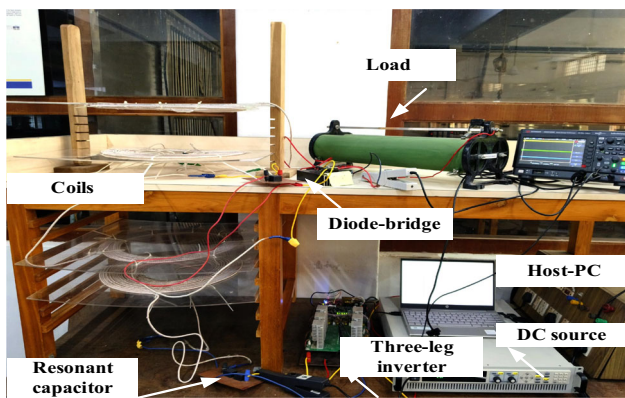


Fig. 5 A laboratory prototype of the proposed dual bridge converter

$$V_{AB} - I_1 Z_1 - j I_3 \omega M_{13} = 0 \tag{13}$$

$$j \omega M_{13} I_1 + \left(Z_3 + \frac{R_{ac}}{2} \right) I_3 = 0 \tag{14}$$

The primary current I_1 for F-B mode is given in (15).

$$I_1 = \frac{V_{AB}}{Z_1 + \frac{(\omega M_{13})^2}{Z_3 + \frac{R_{ac}}{2}}} \tag{15}$$

In the case of half-bridge mode, by applying KVL to Fig. 5, one can obtain (16) and (17).

$$\frac{V_{AB}}{2} - I_1 Z_1 - j I_3 \omega M_{13} = 0 \tag{16}$$

$$j \omega M_{13} I_1 + \left(Z_3 + \frac{R_{ac}}{2} \right) I_3 = 0 \tag{17}$$

$$I_1 = \frac{\frac{V_{AB}}{2}}{Z_1 + \frac{(\omega M_{13})^2}{Z_3 + \frac{R_{ac}}{2}}} \tag{18}$$

The efficiency of V-D, I-D, F-B, and H-B is given in (19), (20), (21), and (22).

$$\eta_v = \frac{R_{ac} |I_3|^2}{V_{AB} |\text{Re}(I_1)| + V_{AC} |\text{Re}(I_2)|} \tag{19}$$

$$\eta_i = \frac{\frac{R_{ac}}{4} |I_3 + I_4|^2}{V_{AB} |\text{Re}(I_1)| + V_{BC} |\text{Re}(I_2)|} \tag{20}$$

$$\eta_{FB} = \frac{\frac{R_{ac}}{2} |I_3|^2}{V_{AB} |\text{Re}(I_1)|} \tag{21}$$

$$\eta_{HB} = \frac{\frac{R_{ac}}{2} |I_3|^2}{\left| \frac{V_{AB}}{2} \text{Re}(I_1) \right|} \tag{22}$$

2.6 Comparison of individual charging system

Typically, individual charging systems are mandated for the task of energizing both 400V and 800V batteries. This entails employing two H-bridge inverters, coupled coils in pairs, and a duo of diode/active bridge rectifiers. Conversely, the proposed system streamlines this process, dispensing with the necessity for active switches and control on the receiving end. This streamlined approach significantly reduces overall complexity compared to existing solutions. The proposed system achieves this efficiency by utilizing fewer components, thereby enhancing cost-effectiveness. For instance, in systems dedicated to charging 400V batteries independently, the total current coursing through coupled coils is twice that of the proposed system. This mandates the usage of higher gauge litz wires. Similarly, systems aimed at charging 800V batteries individually entail twice the voltage across coils, thereby demanding higher cable insulation. However, the overall cost escalation attributed to the coils remains modest. Moreover, existing 400V IPT systems can seamlessly transition to the proposed system with minimal adjustments. This involves augmenting the current design with an additional transmitter coil featuring a semiconductor leg, along with a receiver coil equipped with diodes and an SPDT switch. This retrofitting capability underscores the adaptability and scalability of the proposed system, rendering it a versatile and cost-efficient solution for diverse charging needs.

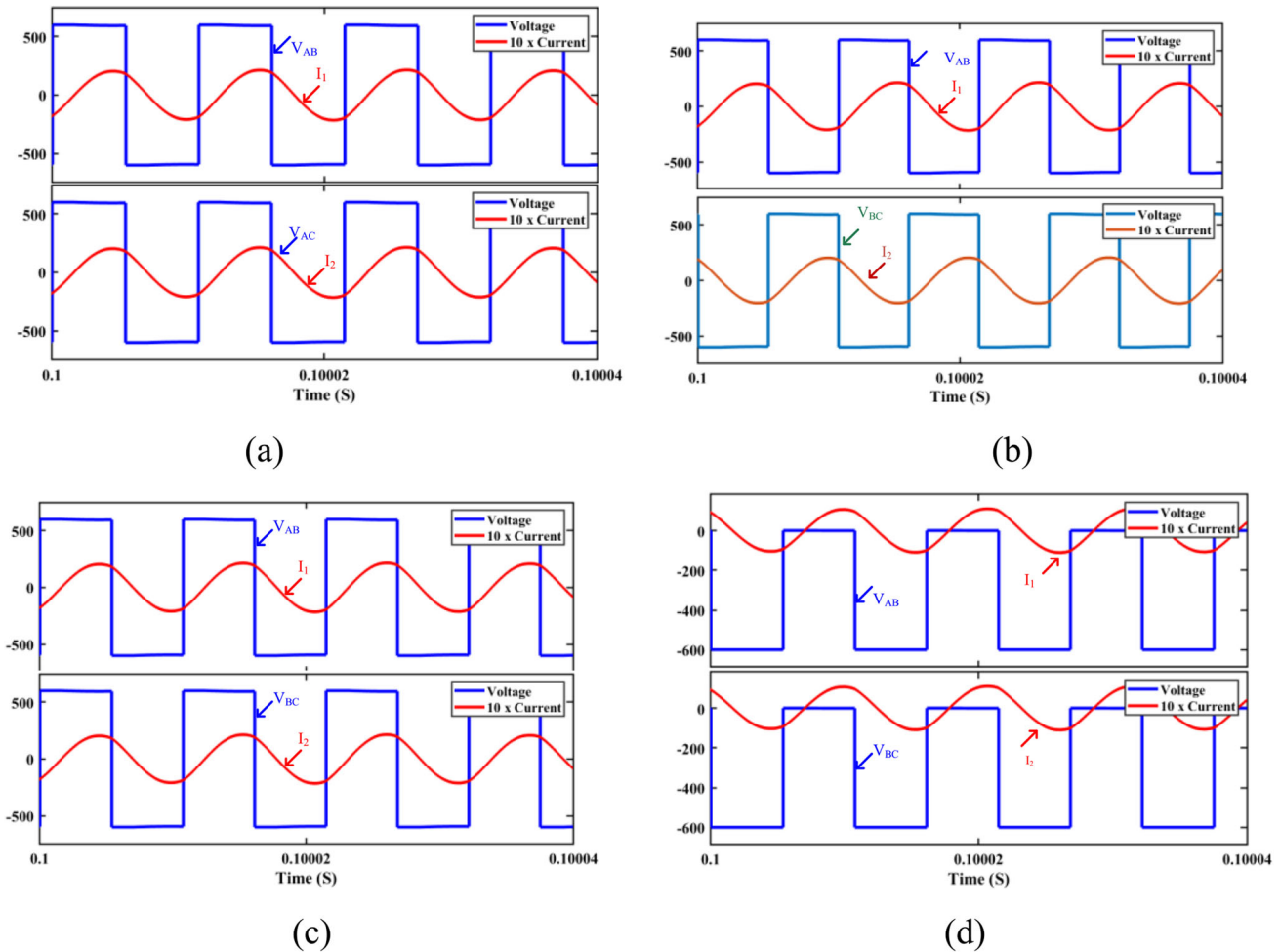
3 Simulation results

The performance validation of the converter was conducted using the MATLAB-Simulink environment, encompassing a comprehensive examination across a wide spectrum of voltage levels. Detailed simulation parameters utilized in the study are presented in Table 1. Figure 6a, b provides visual representations of the inverter’s output voltage and series resonant current flow through the primary coils, elucidating the behavior in both voltage doubler and current doubler modes. In the current doubling mode, the current flowing through the secondary coil is in the reverse direction of voltage doubling mode; because of this, polarity at the secondary coils has been changed, so two coils are connected in parallel effectively. Further insights into the converter’s performance are depicted in Fig. 6c, d, showcasing the voltage and current characteristics of the high-frequency inverter in full-bridge and half-bridge configurations, respectively.

Moving to output characteristics, Fig. 7a illustrates the output voltage (800 V) and current (9A) at a power level of 7.2 kW in voltage doubler mode, while Fig. 7b presents the same parameters at the same power level but double in current at a voltage of 400 V. Additionally, Fig. 7c delves into the performance during full-bridge operation at 3.6 kW,

Table 1 Simulation and prototype parameters of the proposed system

Parameters	$L_1(\mu\text{H})$	$L_3(\mu\text{H})$	$L_2(\mu\text{H})$	$L_4(\mu\text{H})$	$C_1(\text{nF})$	$C_3(\text{nF})$	$C_2(\text{nF})$	$C_4(\text{nF})$
Simulation	329.13	134.91	329.13	134.91	10.6	21.7	10.6	21.7
Hardware	219.3	72.63	219.3	72.63	15	40	15	40

**Fig. 6** Simulation results of the high-frequency inverter voltage and current in different modes: **a** V-D mode, **b** I-D mode, **c** F-B mode, and **d** H-B mode

displaying an output voltage of 400 V and a current of 9 A. Furthermore, Fig. 7d provides valuable insights into the output voltage and current behavior in half-bridge mode at a power level of 0.9 kW.

4 Experimental implementation

4.1 Laboratory prototype

The experimental validation process for the proposed work involved a meticulous series of tests conducted across varying voltage levels, aimed at offering a thorough evaluation of the prototype's performance. Figure 5 visually represents

the experimental setup, showcasing the proposed prototype in its entirety, while Table 1 comprehensively outlines the detailed specifications crucial for understanding the system's components and configurations. The prototype consists of two identical sets of coupled coils, meticulously fabricated using 38 AWG litz wire with an impressive 1050 strands, each with a diameter of 0.1 mm. The transmitter coil, featuring 24 turns, has an inner diameter of 12 cm and an outer diameter of 40 cm. The secondary coil, comprising 11 turns, boasts an inner diameter of 32 cm and an outer diameter of 40 cm. A high-frequency SiC inverter, constructed utilizing CREE CM0120090D switches, ensures robust performance. This is complemented by the selection of primary and secondary resonant capacitors from Vishay's BFC237892103

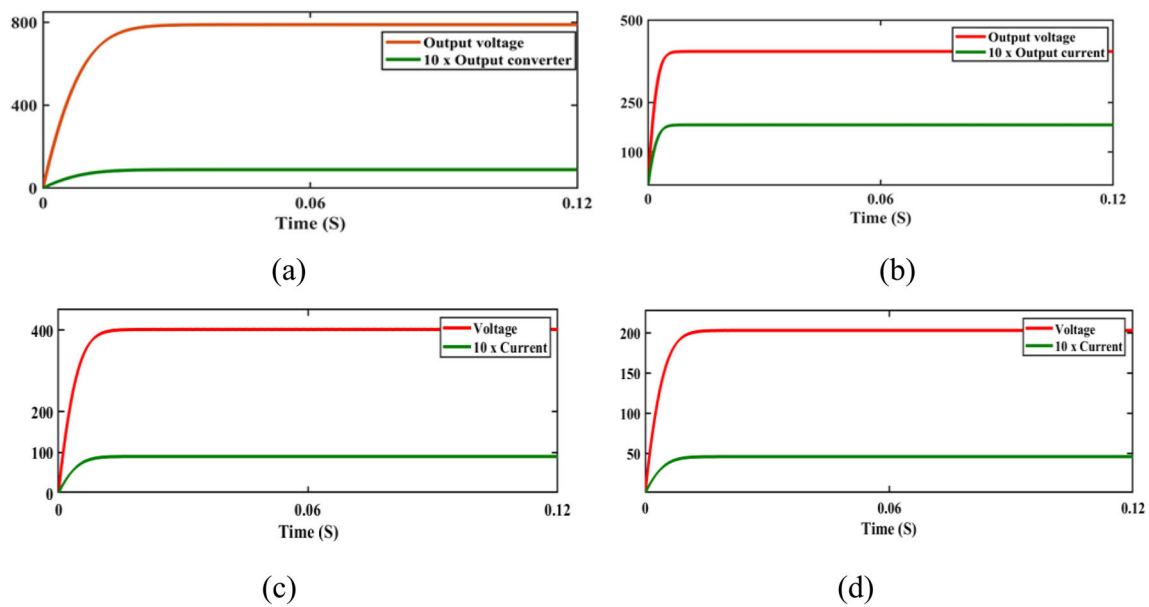


Fig. 7 Simulation results of output voltage and current: **a** V-D mode, **b** I-D mode, **c** F-B mode, and **d** H-B mode

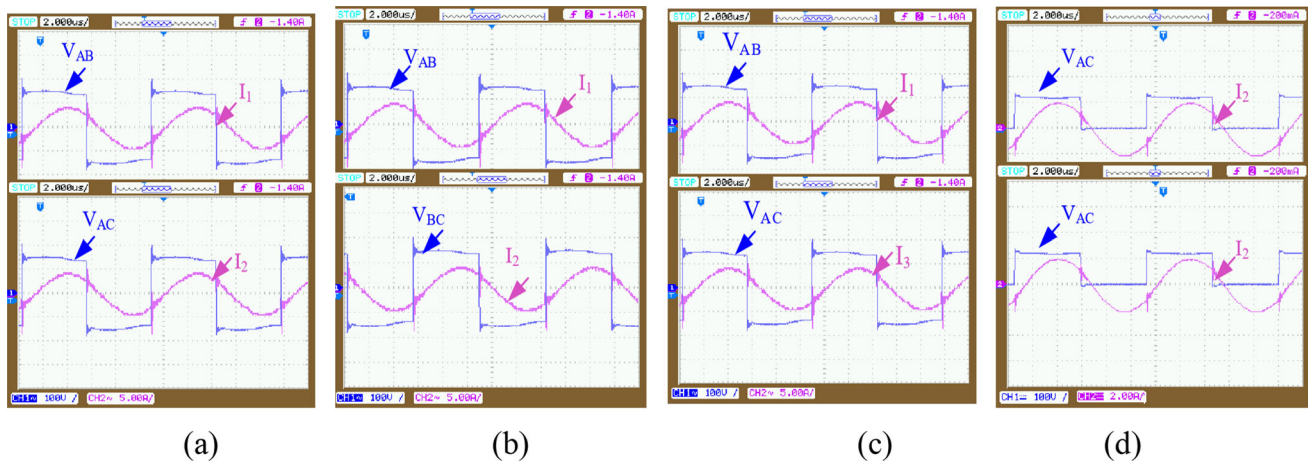


Fig. 8 Experimental results of the high-frequency inverter voltage and current in different modes: **a** V-D mode, **b** I-D mode, **c** individual F-B operation with top and bottom coils, and **d** individual H-B operation with top and bottom coils

series, renowned for their low series equivalent resistance. Additionally, the diode bridge rectifier, integral to the system’s functionality, has been meticulously assembled using DSE 12X101-12A diodes sourced from IXYS. To facilitate control pulses with a 0.5-duty ratio, the TMS320F28379D launch pad was employed, ensuring precise control and management of the system’s operations.

Figures 8 and 9 present detailed insights into the scaled-down experimental results obtained with a vertical distance of 150 mm between the couplers, elucidating the prototype’s performance across different operational modes. Specifically, Fig. 8a, b offers a comprehensive analysis of the inverter voltage and current in two distinct modes: V-D (voltage doubler) and I-D (current doubler), respectively. In V-D

mode, as illustrated in Fig. 9a, the output voltage registers at 100 V with a current of 5 A. The recorded DC–DC efficiency in this mode reaches an impressive peak of 93.5%, showcasing the prototype’s efficiency under such conditions. Conversely, in I-D mode depicted in Fig. 9b, the output voltage halves to 50 V, while the current doubles to 10 A, resulting in a slightly lower DC–DC efficiency of 93.1%. This slight decrease in efficiency in I-D mode can be attributed to the increased conduction of switches. The V-D and I-D modes maintain a consistent power output of 500 W. Figure 8c, d delves into the performance in full-bridge (F-B) and half-bridge (H-B) modes, respectively. In F-B mode, as depicted in Fig. 9c, the output voltage remains steady at 50 V, accompanied by a current of 5 A, resulting in a power level of 250

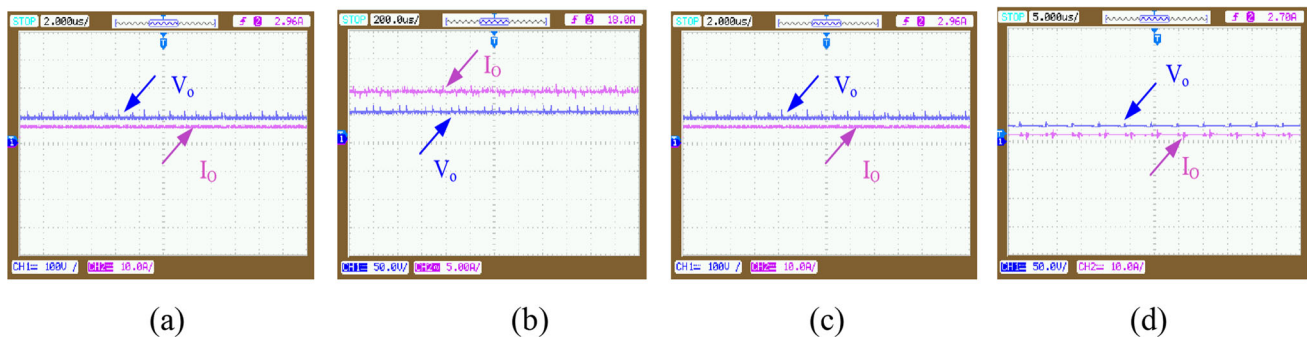


Fig. 9 Experimental results of output voltage and output current in different modes: **a** V-D mode, **b** I-D mode, **c** F-B mode, and **d** H-B mode

W. Remarkably, the measured efficiency in F-B mode stands at 93.3%, underscoring the prototype's robust performance in this configuration. Transitioning to H-B mode, Fig. 9d showcases a reduction in output voltage to 25 V, coupled with a current of 2.5 A. Despite the decrease in power, the prototype maintains a commendable efficiency of 92.6%.

5 Conclusion

This paper introduces a dual full-bridge series-series resonant IPT system designed to accommodate a variety of battery pack voltage ranges without the need for active converters on the secondary side. The operational modes of the proposed system, namely V-D, I-D, F-B, and H-B, are thoroughly elucidated, highlighting its versatility and adaptability. Moreover, the paper outlines the advantages of the proposed system over individual systems, emphasizing its potential to streamline charging processes and reduce complexity. To validate the feasibility of the proposed system, initial verification is conducted through MATLAB/Simulink simulations, demonstrating its effectiveness across different operational modes. Furthermore, a laboratory prototype is developed to empirically validate the system's performance under various battery pack voltages ranging from 100 V to 25 V at different power levels. The recorded efficiencies, ranging from 92.6% to 93.5%, underscore the robustness and reliability of the system, even under varying conditions and loads. Looking ahead, the future scope of this research involves delving deeper into the proposed converter's closed-loop design and control mechanisms, aiming to optimize efficiency and performance further. By continuing to explore and refine these aspects, the proposed system stands poised to offer even greater benefits and advancements in the realm of wireless charging technology.

Author contributions Marupuru Vinod wrote the paper; Dharavath Kishan prepared the figures; and all authors reviewed the manuscript.

Declarations

Competing interests The authors declare no competing interests.

References

- Chen C-J, Chu T-H, Lin C-L, Jou Z-C (2010) A study of loosely coupled coils for wireless power transfer. *IEEE Trans Circuits Syst II Express Briefs* 57(7):536–540
- Xue R-F, Cheng K-W, Je M (2013) High-efficiency wireless power transfer for biomedical implants by optimal resonant load transformation. *IEEE Trans Circuits Syst I Regul Pap* 60(4):867–874
- Al-Saadi M et al (2018) Inductive power transfer for charging the electric vehicle batteries. *Electrotehnica, Electronica, Automatica* 66(4):29
- Patil D, McDonough MK, Miller JM, Fahimi B, Balsara PT (2018) Wireless power transfer for vehicular applications: overview and challenges. *IEEE Trans Trans Electrif* 4(1):3–37
- Ahmad A, Alam MS, Chabaan R (2018) A comprehensive review of wireless charging technologies for electric vehicles. *IEEE Trans Trans Electrif* 4(1):38–63
- “Available:www.evspecifications.com/,” Ev Specifications Accessed on :18/08/2023.
- Jung C (2017) Power up with 800-v systems: the benefits of upgrading voltage power for battery-electric passenger vehicles. *IEEE Electrif Mag* 5(1):53–58
- Ramezani and M. Narimani, “A new wireless ev charging system with integrated dc–dc magnetic element,” *IEEE Transactions on Transportation Electrification*, vol. 5, no. 4, pp. 1112–1123, 2019.
- Zhao L, Thrimawithana DJ, Madawala UK (2017) Hybrid bidirectional wireless ev charging system tolerant to pad misalignment. *IEEE Trans Ind Electron* 64(9):7079–7086
- Hsieh YC, Lin ZR, Chen MC, Hsieh HC, Liu YC, Chiu HJ (2017) High-efficiency wireless power transfer system for electric vehicle applications. *IEEE Trans Circuits Syst II: Express Briefs* 64(8):942–946
- Yang G, Song K, Huang X, Wang C, Huang X, Li J, Zhu C (2021) Improved interoperability evaluation method for wireless charging systems based on interface impedance. *IEEE Trans Power Electron* 36(8):8588–8592
- Gati E, Kampitsis G, Manias S (2017) Variable frequency controller for inductive power transfer in dynamic conditions. *IEEE Trans Power Electron* 32(2):1684–1696
- Cui K, Sun Y, Fan X, Ma Y (2022) A fully integrated single-stage wireless power receiver with phase-shift pwm control for high battery charging resolution. *IEEE Trans Circuits Syst II Express Briefs* 69(9):3679–3683

14. Chen Y, Zhang H, Jin N, Guo L, Wu J, Park SJ, Kim DH (2022) A unipolar-duty-cycle hybrid control strategy of series-series compensated ipt system for constant-current output and efficiency optimization. *IEEE Trans Power Electron* 37(11):13884–13901
15. Liu X, Wang T, Gao F, Khan MM, Yang X, Rogers DJ (2023) A resonant inductor integrated-transformer-based receiver for wireless power transfer systems. *IEEE Trans Industr Electron* 70(4):3616–3626
16. Lu R et al (2022) An efficient DC-DC converter for inductive power transfer in low-power sensor applications. *Int J Circuit Theory Appl* 50(8):2887–2899
17. Wang, Meng, et al. "Design and optimization of hybrid resonant loops for efficient wireless power transfer." *International Journal of Circuit Theory and Applications* 46.2 (2018): 328–342.
18. Tang Yu et al (2022) Research on dual-frequency modulation strategy of wireless power transfer system. *Int J Circuit Theory Appl* 50(12):4342–4356
19. Zhao Yu, Yang S (2022) Voltage control to maximize the transmission efficiency of a multi-input and multi-output wireless power transfer system. *Int J Circuit Theory Appl* 50(10):3293–3306
20. Grazian F, Soeiro TB, Bauer P (2023) Voltage/current doubler converter for an efficient wireless charging of electric vehicles With 400-V and 800-V battery voltages. *IEEE Trans Industr Electron* 70(8):7891–7903
21. Vinod M, Kishan D, Kannan R, Iqbal A, Mohammed Sulthan S (2024) Primary side control strategies for battery charging regulation in wireless power transfer systems for EV applications. *IET Power Electron*. <https://doi.org/10.1049/pel2.12639>

Publisher's Note Springer Nature remains neutral with regard to jurisdictional claims in published maps and institutional affiliations.

Springer Nature or its licensor (e.g. a society or other partner) holds exclusive rights to this article under a publishing agreement with the author(s) or other rightsholder(s); author self-archiving of the accepted manuscript version of this article is solely governed by the terms of such publishing agreement and applicable law.